Bosonic Fourier Transform

Edgar Barriga[4],[1, 2, 3, 4] Camila Muñoz[1,3],[1, 2, 3, 4] Alejandro Muñoz,[1, 2, 3, 4] Pablo Solano[1],[1, 2, 3, 4] Aldo Delgado[1,2],[1, 2, 3, 4] and Carla Hermann-Avigliano[2,3]1, 2, 3, 4

[11] *Departamento de Física, Universidad de Concepción, 160-C Concepción, Chile*
[22] *Millennium Institute for Research in Optics (MIRO), Chile*
[33] *Departamento de Física, Facultad de Ciencias Físicas y Matemáticas, Universidad de Chile, Santiago, Chile*
[44] *Departamento de Física, Facultad de Ciencias, Universidad de Chile, Santiago, Chile*

Lorem ipsum dolor sit amet, consectetuer adipiscing elit. Ut purus elit, vestibulum ut, placerat ac, adipiscing vitae, felis. Curabitur dictum gravida mauris. Nam arcu libero, nonummy eget, consectetuer id, vulputate a, magna. Donec vehicula augue eu neque. Pellentesque habitant morbi tristique senectus et netus et malesuada fames ac turpis egestas. Mauris ut leo. Cras viverra metus rhoncus sem. Nulla et lectus vestibulum urna fringilla ultrices. Phasellus eu tellus sit amet tortor gravida placerat. Integer sapien est, iaculis in, pretium quis, viverra ac, nunc. Praesent eget sem vel leo ultrices bibendum. Aenean faucibus. Morbi dolor nulla, malesuada eu, pulvinar at, mollis ac, nulla. Curabitur auctor semper nulla. Donec varius orci eget risus. Duis nibh mi, congue eu, accumsan eleifend, sagittis quis, diam. Duis eget orci sit amet orci dignissim rutrum.

I. INTRODUCTION

The discrete Fourier transform (DFT), a linear transformation that relates spatial or temporal data encoded in a function to its frequency-domain counterpart, finds wide application across many disciplines [1]. The implementation of DFT in signal analysis flourished through the fast Fourier transforms (FFT) developed in the second half of the twentieth century [2, 3]. The quantum version of the DFT was studied by V. Lyubashenko and S. Majid [4] before any quantum algorithm relied on it, but the work of P. Shor on factoring products of prime numbers [5] by means of a quantum version of the DFT captured the attention of physicists, and the quantum Fourier transform (QFT) became a key ingredient in quantum algorithms [6–8], encompassing diverse applications like image processing [9], solving partial differential equations [10] and Fourier analysis [11, 12], to name a few. The key advantage of QFT operation is its complexity in quantum computers, as it depends on the number of quantum gates and the depth of the circuit [13]. These scale in the order of $\mathcal{O}(n^2)$ and $\mathcal{O}(n)$, respectively, where n is the number of qubits. Cleve et al. [14] comprehensively studied the complexity of the circuit size and depth in the exact QFT implementation and showed theoretical bounds $\mathcal{O}\left(n(\log n)^2 \log\log n\right)$ and $\mathcal{O}(\log n)$, respectively. However, even if we were able to synthesize the optimal circuit to perform QFT, it would not be more efficient than classical computation when the amplitudes of the signal are involved, since measurements introduce a factor 2^n into the complexity [15].

The QFT is not limited to applications in quantum algorithms for quantum computing (digital computing). Its unitary operator inherently describe the photon evolution through photonic integrated circuits (PICs) [16] (analog computing), where it plays an important role in the study of multiphoton interference that allows super-sensitivity for single and multiparameter estimation [17, 18], a new quantum tomography scheme to efficiently characterize optical transformations [19], coherently map photonic states into a qubit register for optical imaging [20], a fundamental component of a universal quantum sorter [21] and being the interferometer to accomplish the certification required in boson sampling by virtue of the suppression law [22].

The PICs to implement any unitary operator are mainly based on the Reck [23] and Clements [24] architectures, but the QFT of size $N = 2^n$ was further optimized by Barak *et al.* [25] by mapping the Cooley-Tukey algorithm in the circuit design, reducing the optical complexity [26] (SU(2) operations) from $\mathcal{O}(N^2)$ to $\mathcal{O}(N \log_2 N)$. This scaling, although improved, is still far from applications beyond proof-of-principle for the photonic QFT, such as proving genuine interference in boson sampling [22], due to the large number of beamsplitter and phase shifters required yet [27, 28].

In this work, we depart from the usual PICs schemes [23–25] and study the evolution of coupled bosonic modes analytically and numerically to obtain the QFT in a single step of interaction, *i. e.*, optical complexity $\mathcal{O}(1)$. Two branches of QFT design are born from our solutions: regular polygon- and graph-based models. In the former model, we find the equations that govern what couplings will lead to the QFT and our calculations reveal that the evolution operator always converges to a complex Hadamard matrix; in the latter, unlike the previous case, different propagation constants must be included in the Hamiltonian to converge the calculations.

This paper is organized as follows. In Sec. II we present analytical solutions up to $N = 6$ modes for a regular polygon waveguide arrangement and give the general equations for this model. In Sec. III we address the limitations of the exponential evanescent coupling decay of the polygon model we introduced in Sec. II, providing new architectures to perform the QFT. Finally, in Sec. IV A we extend the results of Barak *et al.* [25] by mapping the Good-Thomas algorithm to the new building blocks found in Sec. III and in Sec. IV B we introduce Monte Carlo simulations to show the experimental feasibility of

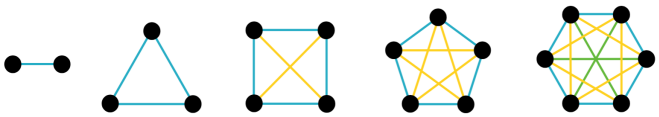

Figure 1. Figura prelimnar. La idea es que se puedan apreciar los acoplamientos. Estos son los casos con solución analítica.

the new architectures.

II. POLYGON MODEL

The interaction between bosonic modes $a_l^\dagger$ in a waveguide array can be described, in the second quantization, through the following Hamiltonian

$$\hat{H} = \hbar \sum_l \beta_l a_l^\dagger a_l + \hbar \sum_{\langle j,k \rangle} \left(C_{jk} a_j^\dagger a_k + C_{jk}^* a_k^\dagger a_j \right) , \quad (1)$$

where β_l is the propagation constant in the l-th waveguide and C_{jk} represents the evanescent coupling between the j-th and k-th modes. The evolution of the annihilation and creation operators is given by a unitary operator U that is obtained as the exponential of the coupling matrix $\mathcal{C}$ in the single particle representation [29], that is,

$$U = e^{-i\mathcal{C}z}, \quad (2)$$

where z is the interaction or propagation length, and

$$\vec{a}' = U\vec{a} \quad (3)$$

with $\vec{a}'$ ($\vec{a}$) a column vector containing the output (input) annihilation modes. For the sake of clarity, hereafter z will be implicitly included in the coefficients β_l and C_{jk}.

The N-dimensional QFT is given by

$$\mathcal{U}^{(N)} = \frac{1}{\sqrt{N}} \begin{pmatrix} 1 & 1 & 1 & \cdots & 1 \\ 1 & \omega & \omega^2 & \cdots & \omega^{N-1} \\ 1 & \omega^2 & \omega^4 & \cdots & \omega^{(N-1)2} \\ 1 & \omega^3 & \omega^6 & \cdots & \omega^{(N-1)3} \\ \vdots & \vdots & \vdots & \ddots & \vdots \\ 1 & \omega^{N-1} & \omega^{2(N-1)} & \cdots & \omega^{(N-1)(N-1)} \end{pmatrix}, \quad (4)$$

where $\omega = e^{-2i\pi/N}$.

From Eq. (2) one may be tempted to calculate the matrix logarithm of Eq. (4), which can be done numerically. Nevertheless, the solutions obtained from this approach cannot be implemented, as this will involve negative couplings. A physically acceptable realization of the QFT can be obtained by supplementing the unitary evolution of Eq. (2) with phase-shifters, that is, with diagonal matrices Φ^{in} and Φ^{out}, before and after the free evolution.

In the case of two waveguides, the unitary transformation can be easily obtained

$$U_2 = \exp \begin{pmatrix} 0 & -i\theta \\ -i\theta & 0 \end{pmatrix} = \begin{pmatrix} \cos\theta & -i\sin\theta \\ -i\sin\theta & \cos\theta \end{pmatrix}, \quad (5)$$

where θ is the coupling coefficient. When the coupling is $\theta = \pi/4$ and the input and output phase-shifter matrices are

$$\Phi^{\text{out}} = \Phi^{\text{in}} = \begin{pmatrix} 1 & 0 \\ 0 & e^{i\pi/2} \end{pmatrix}, \quad (6)$$

we obtain the 2-dimensional QFT, or equivalently, the Hadamard gate, as

$$\Phi^{\text{out}} U_2 \Phi^{\text{in}} = \frac{1}{\sqrt{2}} \begin{pmatrix} 1 & 1 \\ 1 & -1 \end{pmatrix}. \quad (7)$$

From this result, we can see that even in the most simple case, we cannot obtain the QFT directly from Eq. (2). Notice that the factor $1/\sqrt{N}$ in the QFT (4) is not given by an arbitrary choice like in the DFT, where a factor $1/N$ can be put in the inverse operation, hence the modulus of the elements in the QFT must be $1/\sqrt{N}$. We will refer to this as the balancing or normalization condition.

The 3-dimensional QFT was introduced by Żukowski *et al.* [30] in the context of multi-port beamsplitters and was called tritter. Its implementation was based on the pyramid-like design introduced by Reck *et al.* [23]. Later, Spagnolo *et al.* [31] presented a new realization of the tritter based on 3D integrated optical waveguides. This allowed a single-step evolution realization of the 3-dimensional QFT. They solved the Heisenberg equation considering the same coupling for all interactions (balanced multi-port) and found the evolution operator to be given by

$$U_3 = \frac{1}{3} \begin{pmatrix} e^{-2i\theta} + 2e^{i\theta} & e^{2i\theta} - e^{i\theta} & e^{2i\theta} - e^{i\theta} \\ e^{2i\theta} - e^{i\theta} & e^{-2i\theta} + 2e^{i\theta} & e^{2i\theta} - e^{i\theta} \\ e^{2i\theta} - e^{i\theta} & e^{2i\theta} - e^{i\theta} & e^{-2i\theta} + 2e^{i\theta} \end{pmatrix}, \quad (8)$$

where the balancing to $1/\sqrt{3}$ is achieved when $\theta = 2\pi/9$. Selecting phase-shifter matrices as

$$\Phi^{\text{in}} = \Phi^{\text{out}} = \begin{pmatrix} 1 & 0 & 0 \\ 0 & e^{i4\pi/3} & 0 \\ 0 & 0 & e^{i4\pi/3} \end{pmatrix}, \quad (9)$$

the 3-dimensional QFT is generated as

$$\Phi^{\text{out}} U_3 \Phi^{\text{in}} = \frac{1}{\sqrt{3}} \begin{pmatrix} 1 & 1 & 1 \\ 1 & e^{i2\pi/3} & e^{i4\pi/3} \\ 1 & e^{i4\pi/3} & e^{i8\pi/3} \end{pmatrix}. \quad (10)$$

On the other hand, the transformation matrix presented in Eq. (8) can be obtained straightforwardly by means of Eq. (2) with the coupling matrix

$$\mathcal{C} = \begin{pmatrix} 0 & \theta & \theta \\ \theta & 0 & \theta \\ \theta & \theta & 0 \end{pmatrix}, \quad (11)$$

in which case all modes have the same coupling constant.

When we consider the realization of the 4-dimensional QFT by means of a symmetric multi-port of four modes,

known as the quarter [30], a new parameter ϕ appears in the transformation matrix, which is not fixed by balancing to 1/2. In fact, we have

$$U_4 = \frac{1}{2}\begin{pmatrix} 1 & 1 & 1 & 1 \\ 1 & e^{i\phi} & -1 & -e^{i\phi} \\ 1 & -1 & 1 & -1 \\ 1 & -e^{i\phi} & -1 & e^{i\phi} \end{pmatrix}. \tag{12}$$

This phase has been mentioned in experimental works [32–34], however, among all variables that define how photons evolve in a multi-port interferometer, the origin of the phase ϕ remains undisclosed. This phase ϕ appears when we calculate Eq. (2). To appreciate this, let us consider the coupling in the quarter to be θ at the edges and φ on the diagonals, as shown in Figure 1. From this specific geometry, the coupling matrix reads

$$\mathcal{C} = \begin{pmatrix} 0 & \theta & \varphi & \theta \\ \theta & 0 & \theta & \varphi \\ \varphi & \theta & 0 & \theta \\ \theta & \varphi & \theta & 0 \end{pmatrix}, \tag{13}$$

yielding the following transformation matrix

$$U_4 = \frac{e^{-i(2\theta+\varphi)}}{4}\begin{pmatrix} 1+2e^{2i(\theta+\varphi)}+e^{4i\theta} & 1-e^{4i\theta} & 1-2e^{2i(\theta+\varphi)}+e^{4i\theta} & 1-e^{4i\theta} \\ 1-e^{4i\theta} & 1+2e^{2i(\theta+\varphi)}+e^{4i\theta} & 1-e^{4i\theta} & 1-2e^{2i(\theta+\varphi)}+e^{4i\theta} \\ 1-2e^{2i(\theta+\varphi)}+e^{4i\theta} & 1-e^{4i\theta} & 1+2e^{2i(\theta+\varphi)}+e^{4i\theta} & 1-e^{4i\theta} \\ 1-e^{4i\theta} & 1-2e^{2i(\theta+\varphi)}+e^{4i\theta} & 1-e^{4i\theta} & 1+2e^{2i(\theta+\varphi)}+e^{4i\theta} \end{pmatrix}. \tag{14}$$

Balancing the moduli in Eq.(14), implies that

$$1 = |\sin(2\theta)|, \tag{15a}$$
$$0 = |\cos(2\theta)\sin(2\varphi)|, \tag{15b}$$

thus, only θ is relevant to attain normalization, and its value must clearly be $\theta = \pi/4$. As the next step in the search for the 4-dimensional QFT, we need to make the coefficients of the first row and the first column equal to 1. This can be done with the phase-shifter matrices

$$\Phi^{\text{in}} = \text{diag}\left(e^{-i\varphi}, ie^{i\varphi}, -e^{-i\varphi}, e^{i\varphi}\right), \tag{16a}$$
$$\Phi^{\text{out}} = \text{diag}\left(1, ie^{i2\varphi}, -1, ie^{i2\varphi}\right), \tag{16b}$$

leaving us with the transformation

$$\Phi^{\text{out}} U_4 \Phi^{\text{in}} = \frac{1}{2}\begin{pmatrix} 1 & 1 & 1 & 1 \\ 1 & -e^{i4\varphi} & -1 & e^{i4\varphi} \\ 1 & -1 & 1 & -1 \\ 1 & e^{i4\varphi} & -1 & -e^{i4\varphi} \end{pmatrix}. \tag{17}$$

By comparing Eq. (17) with Eq. (12) we can see that the phase ϕ mentioned in Eq. (12) corresponds to the diagonal coupling φ in the quarter array (see Fig. 1). When $\theta = \pi/4$, $\varphi = \pi/8$ and after permuting the second with the fourth column in Eq. (17), we finally obtain the 4-dimensional QFT. In this context, permutations of columns (rows) mean that waveguides must be swapped before (after) the interaction occurs.

From the perspective of graph theory, the coupling matrices we have studied so far correspond to a complete graph, that is, a graph where every vertex is connected to every other vertex. Ahmadi *et al.* [35] demonstrated that instantaneous uniform mixing, that is, having $|U^{(N)}_{m,n}| = 1/\sqrt{N}$ [36], is possible only for $N = 2,\ 3,\ 4$ in complete graphs. This result implies that we have to relinquish the idea of finding the QFT through complete-graph-like coupling matrices.

Notwithstanding this mathematical theorem, we achieved the 5-dimensional QFT from the coupling matrix

$$\mathcal{C} = \begin{pmatrix} 0 & \theta & \varphi & \varphi & \theta \\ \theta & 0 & \theta & \varphi & \varphi \\ \varphi & \theta & 0 & \theta & \varphi \\ \varphi & \varphi & \theta & 0 & \theta \\ \theta & \varphi & \varphi & \theta & 0 \end{pmatrix}, \tag{18}$$

which represent the interactions in the pentagon arrangement (see Figure 1) and corresponds to a complete graph. The complex exponential of $\mathcal{C}$ (18) provides the squares moduli

$$\left|U^{(5)}_{1,1}\right|^2 = \frac{1}{25}\left[9 + 8\cos\left(\sqrt{5}(\theta-\varphi)/2\right)\cos\left(5(\theta+\varphi)/2\right) + 8\cos\left(\sqrt{5}(\theta-\varphi)\right)\right], \tag{19a}$$

$$\left|U^{(5)}_{1,2}\right|^2 = \frac{2}{25}\left[2 + \sqrt{5}\sin\left(5(\theta+\varphi)/2\right)\sin\left(\sqrt{5}(\theta-\varphi)/2\right) - \cos\left(5(\theta+\varphi)/2\right)\cos\left(\sqrt{5}(\theta-\varphi)/2\right) - \cos\left(\sqrt{5}(\theta-\varphi)\right)\right], \tag{19b}$$

$$\left|U^{(5)}_{1,3}\right|^2 = \frac{2}{25}\left[2 - \sqrt{5}\sin\left(5(\theta+\varphi)/2\right)\sin\left(\sqrt{5}(\theta-\varphi)/2\right) - \cos\left(5(\theta+\varphi)/2\right)\cos\left(\sqrt{5}(\theta-\varphi)/2\right) - \cos\left(\sqrt{5}(\theta-\varphi)/2\right)\right], \tag{19c}$$

where $U^{(5)}_{14} = U^{(5)}_{13}$, $U^{(5)}_{15} = U^{(5)}_{12}$ and the remaining rows of $U^{(5)}$ are cyclically shifted to the right from the preced-

ing. The system of equations $|U^{(5)}_{jk}|^2 = 1/5$ is reduced to

$$0 = \sin\left(\frac{\sqrt{5}}{2}(\theta-\phi)\right)\sin\left(\frac{5}{2}(\theta+\phi)\right), \tag{20a}$$

$$0 = \cos^2\left(\sqrt{5}(\theta-\phi)/2\right) - \frac{1}{2}\cos\left(\sqrt{5}(\theta-\phi)/2\right) - \frac{1}{4}, \tag{20b}$$

with one particular solution being

$$\theta = \frac{\pi\left(5+\sqrt{5}\right)}{25}, \tag{21a}$$

$$\varphi = \frac{\pi\left(5-\sqrt{5}\right)}{25}. \tag{21b}$$

Other solutions are available due to the periodicity of trigonometric functions in $2\pi k$. It is important not to overlook which integer k is chosen, as the length of the interaction and the strength of the coupling are determined by this choice. A non intuitive consequence also emerges from this choice, which is the presence of permutation matrices. For the solutions represented in Eq. (21), no permutation matrices are required, and the QFT is realized just with the phase-shifter matrices

$$\Phi_5^{\text{in}} = \text{diag}\left(e^{-i\pi/5}, e^{3i\pi/5}, e^{i\pi}, e^{i\pi}, e^{3i\pi/5}\right), \tag{22a}$$

$$\Phi_5^{\text{out}} = \text{diag}\left(1, e^{4i\pi/5}, e^{-4i\pi/5}, e^{-4i\pi/5}, e^{4i\pi/5}\right), \tag{22b}$$

but for other choices of $2\pi k$, permutation matrices might be necessary.

The previous result for the 5-dimensional QFT motivates us to examine a general polygon model. Since the distances between the vertices of a regular polygon are cyclic, the general coupling matrix is circulant, that is, all rows are composed of the same elements, and each row is rotated one element to the right relative to the preceding row. Thereby, the coupling matrix becomes

$$\mathcal{C} = \begin{pmatrix} 0 & C_1 & C_2 & \cdots & C_{N-2} & C_{N-1} \\ C_{N-1} & 0 & C_1 & \cdots & C_{N-3} & C_{N-2} \\ \vdots & \vdots & \vdots & \ddots & \vdots & \vdots \\ C_2 & C_3 & C_4 & \cdots & 0 & C_1 \\ C_1 & C_2 & C_3 & \cdots & C_{N-1} & 0 \end{pmatrix}. \tag{23}$$

Circulant matrices are diagonalized through the discrete Fourier matrix F, allowing us to determine $U^{(N)}$ as

$$e^{-i\mathcal{C}z} = F^\dagger e^{-i\Lambda z} F, \tag{24}$$

where Λ is the diagonal matrix that contains the eigenvalues λ_k of $\mathcal{C}$. Consequently, the coefficients of $U^{(N)}$ are expressed as

$$U^{(N)}_{m,n} = \frac{1}{N}\sum_{k=0}^{N-1}\exp\left(2\pi i k(n-m)/N - i\lambda_k\right). \tag{25}$$

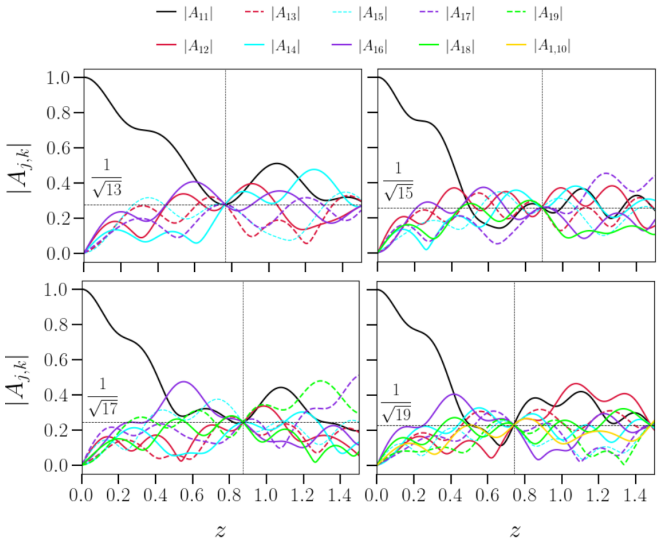

Figure 2. Moduli of U for $N = 13, 15, 17, 19$ solved from Eq. (27) and Eq. 28. Figura preliminar

In a regular polygon of S sides, we have $\lfloor S/2 \rfloor$ different distances, so the evanescent coupling strength felt by the waveguides has symmetry $C_l = C_{N-l}$ for $l = 1, \cdots, N-1$. Thus, the eigenvalues of $\mathcal{C}$ (23) are given by

$$\lambda_k = C_0 + 2\sum_{l=1}^{(N-1)/2} C_l \cos\left(2\pi k l/N\right), \tag{26a}$$

$$\lambda_k = C_0 + C_{N/2}\cos\left(k\pi\right) + 2\sum_{l=1}^{N/2-1} C_l \cos\left(2\pi k l/N\right). \tag{26b}$$

Eq. (26a) and Eq. (26b) correspond to the eigenvalues when N is odd or even, respectively. These have symmetry $\lambda_k = \lambda_{N-k}$ for $1 \le k \le \lceil N/2 \rceil - 1$.

The normalization condition over $U^{(N)}_{mn}$ (25) is captured by the following equation (see Appendix B for details)

$$0 = \sum_{j=1}^{N-1}\sum_{k=j}^{N-1}\cos\left(\frac{2\pi j(m-n)}{N} + \lambda_k - \lambda_{k-j}\right). \tag{27}$$

A solution to Eq. (27) does not guaranty that we have found the QFT, but would provide a complex Hadamard matrix [37]. To ensure that $U^{(N)}$ (25) is the N-dimensional QFT (4), the core of the dephased form of $U^{(N)}$, that is, the submatrix $U^{(N)}_{jk}$, $j,k = 1, \cdots, N-1$ (core) when $U^{(N)}_{0,j} = U^{(N)}_{j,0} = 1$ (dephased), must coincide with Eq. (4). This constrains the solutions of Eq. (27) to also fulfill the equation (see Appendix B for details)

$$0 = \sum_{j,k,l,p=0}^{N-1}\sin\left((k-l)\frac{2\pi n}{N} + (j-k)\frac{2\pi m}{N} + \lambda_{jklp}\right), \tag{28}$$

where $\lambda_{jklp} = \lambda_j - \lambda_k + \lambda_l + \lambda_p$. The dephased version of $U^{(N)}$, which is denoted by $\mathcal{D}^{(N)}$, is then given by

$$\mathcal{D}^{(N)} = \Phi^{\text{out}} U^{(N)} \Phi^{\text{in}}, \tag{29a}$$

$$\Phi^{\text{in}} = \text{diag}\left(u_{0,0}^{(N)*}, \cdots, u_{0,n}^{(N)*}, \cdots, u_{0,N-1}^{(N)*}\right), \tag{29b}$$

$$\Phi^{\text{out}} = \text{diag}\left(1, u_{1,0}^{(N)*}, \cdots, u_{m,0}^{(N)*}, \cdots, u_{N-1,0}^{(N)*}\right), \tag{29c}$$

where $u_{mn}^{(N)} = \sqrt{N} U_{mn}^{(N)}$.

It is important to note that $\exp(-i\mathcal{C}z)$ inherits the same circulant structure $\mathcal{C}$ (23) has, and therefore we only need to solve Eq. (27) for $m = 0$ and $n = 0, \cdots, \lfloor (N-1)/2 \rfloor$ and check the solution in Eq. (28).

We analytically solved Eq. (27) for the hexagonal geometry (see Fig. 1) which leads to the set of coupling constants (see Appendix A for details)

$$C_1 = \frac{\pi}{3} + \frac{\pi}{3}(k_1 + k_2), \tag{30a}$$

$$C_2 = \frac{\pi}{9} + \frac{\pi}{3}(k_1 - k_2), \tag{30b}$$

$$C_3 = \frac{\pi}{12} - \frac{\pi}{6}(k_1 + k_2 - 3k_3). \tag{30c}$$

The integers k_1, k_2 and k_3 can be freely chosen, but

When $k_1 = 0$, $k_2 = 0$ and $k_3 = 0$, we have

$$\Phi^{\text{in}} = \text{diag}\left(e^{-i5\pi/18}, e^{i5\pi/9}, e^{-i17\pi/18}, e^{-i7\pi/9}, e^{-i17\pi/18}, e^{i5\pi/9}\right) \tag{31}$$

$$\Phi^{\text{out}} = \text{diag}\left(1, e^{i5\pi/6}, e^{-i2\pi/3}, e^{-i1\pi/2}, e^{-i2\pi/3}, e^{i5\pi/6}\right) \tag{32}$$

C_1 vanishes when $k_1 = 0$, $k_2 = -1$ and $k_3 = 1$

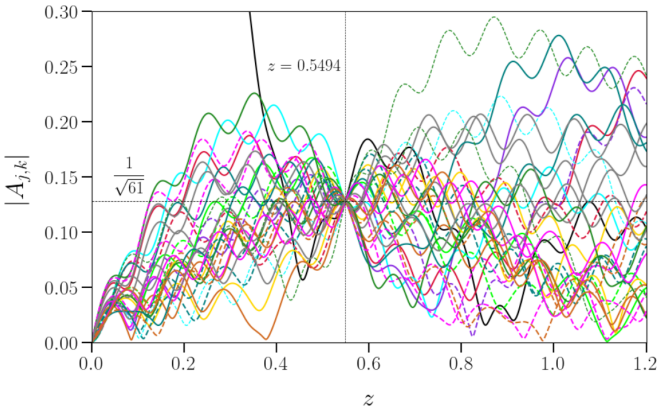

Figure 3. Complex Hadamard matrix for $N = 61$. La idea es mostrar un caso de N grande para que se vea lo general de la solucion (no hemos demostrado que funciona para cualquier N) y que la QFT se vuelve esquiva de encontrar a diferencia de las Hadamard que salen a cada rato

Although general, this solution struggles with distance between non-adjacent waveguides as we add more waveguides.

$$\kappa \propto e^{-\gamma r} \tag{33}$$

$$\frac{\ln(\kappa_1/\kappa_2)}{r_2 - r_1} = \gamma \tag{34}$$

If we consider a waveguide with diameter 10 μm, then $\gamma r_1 \approx 5.5$, for $r_1 = 20\ \mu\text{m}^{-1}$, $\gamma \approx 0.275$.

III. ANOTHER QFT ARCHITECTURES

To address the inexorable limitations of the polygon model regarding the decaying coupling strength, we explored new configurations of interactions among the waveguides. Multiarm interferometers can be seen as a graph, where the vertices correspond to the waveguides, and the edges represent the couplings. In our case, the label of the waveguides is not relevant; therefore, all possible configurations are mapped to the number of simple connected graphs on N unlabeled vertices; hence, there are 2, 6, 21, 112 and 853 different setups of interferometers for $N = 3, 4, 5, 6, 7$, respectively. For three waveguides, the two possible dispositions are the tritter and the nearest-neighbor line. The tritter leads to the QFT [31], the line does not, since it is not possible to balance the moduli in its transformation matrix even when the couplings are different (see Appendix C in [38]). Notwithstanding, if we take the propagation constant into account, the 3-mode QFT is within reach for the latter waveguide layout when we assign β to the central waveguide. In this case, the transformation matrix elements are given by

$$U_{1,1}^{\#1} = \frac{1}{2} + \frac{e^{-i\beta/2}}{2\Theta}\left(\Theta\cos(\Theta/2) + \beta\sin(\Theta/2)\right) \tag{35a}$$

$$U_{1,2}^{\#1} = -\frac{2i\theta}{\Theta} e^{-i\beta/2}\sin(\Theta/2) \tag{35b}$$

$$U_{1,3}^{\#1} = -\frac{1}{2} + \frac{e^{-i\beta/2}}{2\Theta}\left(\Theta\cos(\Theta/2) + \beta\sin(\Theta/2)\right) \tag{35c}$$

$$U_{2,2}^{\#1} = e^{-i\beta/2}\left(\cos(\Theta/2) - i\frac{\beta}{\Theta}\sin(\Theta/2)\right), \tag{35d}$$

$$\Theta = \sqrt{\beta^2 + 8\theta^2}, \tag{35e}$$

where $|U_{33}^{\#1}| = |U_{11}^{\#1}|$ and $|U_{23}^{\#1}| = |U_{12}^{\#1}|$. When we balance the moduli in Eq.(35) to $1/\sqrt{3}$ the resulting equations are transcendental. Unlike the tritter, a permutation between the second and third column is now necessary. The 3-mode QFT appears again when we include β_l in the tritter, the matrix elements are listed in the Appendix C. In Figure 4 we show the new designs.

Although the new configurations for the 3-mode QFT would require more engineering in the optical circuit, the incorporation of the propagation constant into the bosonic dynamics reveals that β_l is another relevant variable in the circuit in the course of finding the QFT. When we explored the role of β_l in the 4-dimensional case

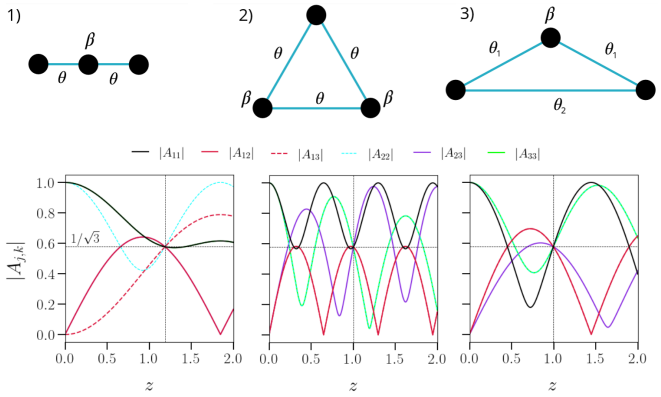

Figure 4. New configurations of three waveguides that lead to the QFT. Now the propagation constant is not the same among the waveguides.

we discovered a new complex Hadamard matrix, which is a surprising result, since all complex Hadamard matrices of dimension 4 are suppose to be determined by Eq. 12 [39]. The structure of the new complex Hadamard matrix found is given by

$$M = \frac{1}{2}\begin{pmatrix} 1 & 1 & 1 & 1 \\ 1 & e^{i\delta} & -1 & -1 \\ 1 & -1 & e^{i\delta} & -1 \\ 1 & -1 & -1 & e^{i\delta} \end{pmatrix}. \tag{36}$$

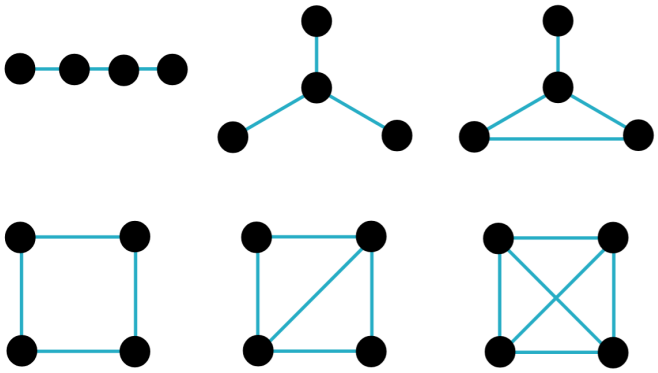

Figure 5. Non isomorphic waveguide arrangement of four waveguides.

The six dissimilar dispositions of four waveguides are shown in Figure 5. The new complex Hadamard matrix comes from the array b) in Figure 5, and with a coupling matrix

$$\mathcal{C} = \begin{pmatrix} \beta & \theta & \theta & \theta \\ \theta & 0 & 0 & 0 \\ \theta & 0 & 0 & 0 \\ \theta & 0 & 0 & 0 \end{pmatrix}, \tag{37}$$

yields the following transformation matrix elements

$$U_{11} = e^{-i\beta/2}\left(\cos(\Theta/2) - i\beta\frac{\sin(\Theta/2)}{\Theta}\right), \tag{38a}$$

$$U_{12} = -2i\theta e^{i\beta/2}\frac{\sin(\Theta/2)}{\Theta}, \tag{38b}$$

$$U_{22} = \frac{e^{-i(\beta+\Theta)/2}}{6\Theta}\left(\Theta - \beta + e^{i\Theta}(\Theta+\beta) + 4\Theta e^{i(\Theta+\beta)/2}\right), \tag{38c}$$

$$U_{23} = \frac{e^{-i(\beta+\Theta)/2}}{6\Theta}\left(\Theta - \beta + e^{i\Theta}(\Theta+\beta) - 2\Theta e^{i(\theta+\beta)/2}\right), \tag{38d}$$

$$\Theta = \sqrt{12\theta^2 + \beta^2}. \tag{38e}$$

where $U_{33} = U_{44} = U_{22}$, $U_{13} = U_{14} = U_{12}$ and $U_{24} = U_{34} = U_{23}$. Imposing $|U_{mn}|^2 = 1/4$ on Eq.38 will clearly engender transcendental equations, therefore, the solutions are numerical and we found $\delta = 0.00257$ for $\theta = 2.599$ and $\beta = 4.322$. This new transformation matrix has new interference effects when we compared it to the 4-dimensional QFT and the Sylvester matrix ($\phi = 0$ in Eq. 12). The theoretical output probabilities for two photons coming in two adjacent waveguides are reported in Table I.

Table I. Output probabilities for an input state $|1,1,0,0\rangle$ after the evolution carry out by U in Eq.(17), (14) ($\phi = 0$) and (36). All of the transformations have 12.0% probability when bunching occurs.

Final state	4-dimensional QFT	Sylvester	New Hadamard
$\langle 1,1,0,0|$	12.5 %	0.0 %	25.0 %
$\langle 1,0,1,0|$	0.0 %	25.0 %	0.0 %
$\langle 1,0,0,1|$	12.5 %	0.0 %	0.0 %
$\langle 0,1,1,0|$	12.5 %	0.0 %	0.0 %
$\langle 0,1,0,1|$	0.0 %	25.0 %	0.0 %
$\langle 0,0,1,1|$	12.5 %	0.0 %	25.0 %

To explore the scenery of finding the QFT in five waveguides, we need to rely on numerical calculations, since as the number of couplings increases, analytical solutions become intractable. To address the problem, we constructed a real multivariate vector-valued function $\vec{f}$ defined as the vectorization

$$\vec{f}(\{\beta_l, C_{jk}\}) = \mathrm{vec}_{\{R\}}\left(e^{-i\mathcal{C}z} \odot e^{i\mathcal{C}z} - \frac{1}{N}\mathbb{J}\right), \tag{39}$$

where $\odot$ indicates the entrywise product, $\mathbb{J}$ is the all-ones matrix, and $\{R\}$ denotes the set of non-repeated matrix elements determined by the symmetries in C_{jk} and β_l. In order to find the couplings, we sought the roots of $\vec{f}(\{\beta_l, C_{jk}\})$ by minimizing its Euclidean norm.

We analytically solved that the pentagon (see Figure 1) can perform the QFT. For the remaining twenty waveguide dispositions (see Figure 6) we proceeded numerically through Eq. (39). Disregarding the propagation constant, none of these twenty candidates conducted

us to the QFT, since a simultaneous modulus of $1/\sqrt{5}$ was never achieved. However, with β included in the coupling matrix, the arrangements 9, 12, 15, 17 and 21 shown in Figure 6 converged to $\mathcal{U}^{(5)}$. Acá me falta informar en qué guías de onda de cada arreglo β está presente. Idea: poner en color la guia de onda que lleva beta

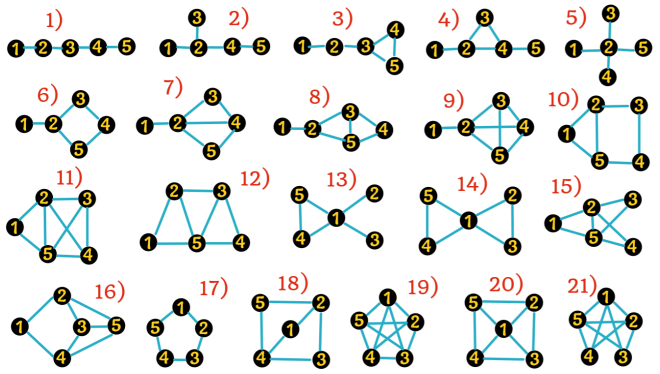

Figure 6. Figura preliminar para mostrar todos los arreglos con 5 guias de onda. De acá referenciaremos cuales dan lugar a la QFT al incluir la optimización de la constante de propagación

Acá continúa la exploración de los diferentes arreglos de guías de onda basados en teoría de grafos. La idea es finalizar esta sección mencionando que abordar los casos de N es complejo numericamente debido a las fases libres y que en el caso de de N impar el problema se vuelve super desiante por el numero de posibles arreglos es inmanejable

A graphical representation of the 121 simple, connected and unlabeled graph of six vertices can be consulted in [40]

Although we have the equations that the couplings must satisfy in order for them to be the QFT, the free phases represent a challenge for the numerical solutions based on Eq. (39). This happens because free phases are a continuous variable, so numerical routines will converge to the first value it finds, even if we impose restraint on the C_l variables. This can be clearly seen in Eq. (15), where the diagonal coupling φ can take any value and does not alter the normalization. Nevertheless, we found the 6-dimensional QFT

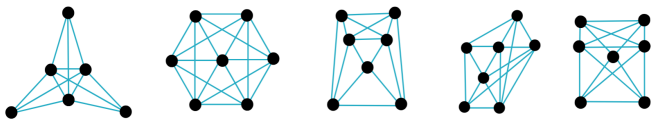

Figure 7. Acá se muestra el único caso en $N = 6$ que da la QFT y los arreglos para $N = 7$ que numericamente dan la QFT.

As we mentioned before, When we face the case of seven waveguides, there are 853 possible configurations,

IV. NEW DESIGNS AND FEASIBILITY

A. Fast Fourier transform algorithms

Esta sección es un spin-off. El punto aca es dar a conocer que la QFT se puede construir a partir de blques de menor dimension.

Cooley-Tukey

$$F = P^{-1}(4,2)\,(\mathbb{I}_2 \otimes F_2)\,T_2(4)\,(F_2 \otimes \mathbb{I}_2) \tag{40}$$

Good-Thomas

$$F_N = P_1\,(F_{N_1} \otimes \mathbb{I}_{N_2})\,(\mathbb{I}_{N_1} \otimes F_{N_2})\,P_2 \tag{41}$$

B. Coupling robustness

La idea aca es mostrar la fidelidad que tendran los arreglos de guias de onda que hemos encontrado para la QFT y abordar brevemente lo de las diferentes plataformas donde estas QFT pueden ser implementadas (esto último podría no ir la verdad)

To evaluate the practical feasibility of the proposed single-step QFT architectures, we analyze their robustness against fabrication imperfections in the propagation constants and coupling coefficients. The parameters used in the simulations were anchored to experimentally reported values in integrated photonics and fiber-based systems, ensuring a realistic representation of current technologies. The propagation constant of each waveguide, $\beta = k_0 n_{\text{eff}} = 2\pi n_{\text{eff}}/\lambda$, lies in the range $\beta \sim$ 4–9 $\times\, 10^6$ m^{-1} for silica-based platforms operating at $\lambda =$ 0.8–1.55 μm [27, 41]. Femtosecond-laser-written circuits exhibit relative variations of 0.5–1% in n_{eff}, which translate into small phase mismatches that can modify the interference pattern of the implemented transformation [41**?**]. The evanescent coupling between adjacent guides follows $C \propto e^{-\gamma r}$ [**?**]. Experiments report coupling lengths of $L_c \approx 2$ mm, corresponding to $C = \pi/(2L_c) \approx 0.8$ mm^{-1} [31, 33]. By varying the separation and interaction length, coupling coefficients within $C =$ 0.1–1.0 mm^{-1} can be engineered [27, 32]. In microfibers and nanofibers, the modal overlap modifies C from 0.05–0.5 mm^{-1} up to 1–10 mm^{-1} for submicrometric gaps [42]. Fabrication-induced deviations were modeled as Gaussian perturbations...

$$\text{fid} = \left|\text{tr}\left(U_{\text{teo}} U_{\text{pert}}^{\dagger}\right)\right|/N \tag{42}$$

El modelo de juguete

- Guias de onda con diametro de 10 μm
- Separacion entre guias de onda: 10 μm
- Error en los acoplamientos: 5-10%
- Error en la constante de propagagación: 1%

- Error en la largo de interaccion: ?
- Para la simulación montecarlo: the bin size is determined by the Freedman-Diaconis rule

V. CONCLUSIONS AND OUTLOOK

- Nosotros hemos mostrado que teoricamente es posible diseñar circuitos ópticos con sólo paso de profundidad para llevar a cabo la QFT y la Hadamard.
- Extendimos la propuesta de Barak y con esto mostramos que el algoritmo de Good-Thomas es también otra receta a seguir ahora que sabemos como hacer la QFT para $M > 3$
- Nosotros estudiamos el acoplamiento con criterio de distancia. Acoplamientos negativos no fueron incluidos en la optimización.

ACKNOWLEDGMENTS

Gracias

Appendix A: 6-dimensional QFT

$$0 = 2 + 2\cos(\lambda_1 - \lambda_0) + 2\cos(\lambda_2 - \lambda_0) + \cos(\lambda_3 - \lambda_0) + 2\cos(\lambda_3 - \lambda_1) + 2\cos(\lambda_3 - \lambda_2) + 4\cos(\lambda_2 - \lambda_1) \quad \text{(A.1a)}$$
$$0 = 1 - \cos(\lambda_1 - \lambda_0) + \cos(\lambda_2 - \lambda_0) + \cos(\lambda_3 - \lambda_0) + \cos(\lambda_3 - \lambda_1) - \cos(\lambda_3 - \lambda_2) + \cos(\lambda_2 - \lambda_1) \quad \text{(A.1b)}$$
$$0 = 1 + \cos(\lambda_1 - \lambda_0) + \cos(\lambda_2 - \lambda_0) - \cos(\lambda_3 - \lambda_0) + \cos(\lambda_3 - \lambda_1) + \cos(\lambda_3 - \lambda_2) - \cos(\lambda_2 - \lambda_1) \quad \text{(A.1c)}$$
$$0 = 2 - 2\cos(\lambda_1 - \lambda_0) + 2\cos(\lambda_2 - \lambda_0) - \cos(\lambda_3 - \lambda_0) + 2\cos(\lambda_3 - \lambda_1) - 2\cos(\lambda_3 - \lambda_2) - 4\cos(\lambda_2 - \lambda_1) \quad \text{(A.1d)}$$

La siguiente ecuacion no se decude, se impone.

$$\cos(\lambda_2 - \lambda_0) = -\frac{1}{2}, \quad \text{(A.2)}$$
$$\cos(\lambda_3 - \lambda_1) = -\frac{1}{2}, \quad \text{(A.3)}$$

$$3(C_1 + C_2) = \frac{4\pi}{3} + 2\pi k_1, \quad \text{(A.4)}$$
$$3(C_1 - C_2) = \frac{2\pi}{3} + 2\pi k_2, \quad \text{(A.5)}$$
$$\implies C_1 = \frac{\pi}{3}, \quad C_2 = \frac{\pi}{9} \quad \text{(A.6)}$$

implies

$$\cos(\lambda_3 - \lambda_2 + \lambda_1 - \lambda_0) = 0, \quad \text{(A.7)}$$
$$\cos(2C_3 + C_1) = 0 \quad \text{(A.8)}$$
$$2C_3 + C_1 = \frac{\pi}{2} + k_3\pi \quad \text{(A.9)}$$
$$\implies C_3 = \frac{\pi}{12} \quad \text{(A.10)}$$

Appendix B: Angle

$$U_{m,n} = \frac{1}{N}\sum_{k=0}^{N-1} e^{2\pi i(n-m)k/N - i\lambda_k} \quad \text{(B.1)}$$
$$= \frac{1}{\sqrt{N}} \exp\left(i \arctan\left(\frac{\sum_k \sin(k(x-y) - \lambda_k)}{\sum_k \cos(k(x-y) - \lambda_k)}\right)\right) \quad \text{(B.2)}$$

$$a = \frac{\sum_{j=0}^{N-1} \sin(jy + \lambda_j)}{\sum_{j=0}^{N-1} \cos(jy + \lambda_j)}, \quad \text{(B.3)}$$

$$b = \frac{\sum_{k=0}^{N-1} \sin(kx - ky - \lambda_k)}{\sum_{k=0}^{N-1} \cos(kx - ky - \lambda_k)}, \quad \text{(B.4)}$$

$$c = -\frac{\sum_{l=0}^{N-1} \sin(lx - \lambda_l)}{\sum_{l=0}^{N-1} \cos(lx - \lambda_l)}, \quad \text{(B.5)}$$

$$d = \frac{\sum_{p=0}^{N-1} \sin(\lambda_p)}{\sum_{p=0}^{N-1} \cos(\lambda_p)} \quad \text{(B.6)}$$

$$\arctan(a) + \arctan(b) + \arctan(c) + \arctan(d) = \arctan\left(\frac{a + b + c + d - abc - abd - acd - bcd}{1 - ab - ac - bc - ad - bd - cd + abcd}\right) \quad \text{(B.7)}$$

$$0 = \mathrm{T}(1 - ab - ac - bc - ad - bd - cd + abcd) \quad \text{(B.8)}$$
$$- a - b - c - d + abc + abd + acd + bcd, \quad \text{(B.9)}$$
$$\mathrm{T} = \tan(-2\pi mn/N) \quad \text{(B.10)}$$

$$
\begin{aligned}
0 = \mathrm{T}(&a_2b_2c_2d_2 - a_1b_1c_2d_2 + a_1b_2c_1d_2 + a_2b_1c_1d_2 \\
&- a_1b_2c_2d_1 - a_2b_1c_2d_1 + a_2b_2c_1d_1 - a_1b_1c_1d_1) \\
&- a_1b_2c_2d_2 - a_2b_1c_2d_2 + a_2b_2c_1d_2 - a_2b_2c_2d_1 \\
&- a_1b_1c_1d_2 + a_1b_1c_2d_1 - a_1b_2c_1d_1 - a_2b_1c_1\delta 1
\end{aligned} \tag{B.11}
$$

$$
\begin{aligned}
a_2b_2c_2 &= \cos(jx-\lambda_j)\cos(kx-ky-\lambda_k)\cos(ly-\lambda_l) \\
&= \frac{1}{4}\Big[\cos\big((j+k)x+(l-k)y-\lambda_j-\lambda_k+\lambda_l\big) \\
&\quad + \cos\big((j+k)x-(k+l)y-\lambda_j-\lambda_k-\lambda_l\big) \\
&\quad + \cos\big((j-k)x+(k+l)y-\lambda_j+\lambda_k+\lambda_l\big) \\
&\quad + \cos\big((j-k)x+(k-l)y-\lambda_j+\lambda_k-\lambda_l\big)\Big]
\end{aligned} \tag{B.12}
$$

$$
\begin{aligned}
a_1b_1c_2 &= \sin(jx-\lambda_j)\sin(kx-ky-\lambda_k)\cos(ly-\lambda_l) \\
&= \frac{1}{4}\Big[\cos\big((j-k)x+(k+l)y-\lambda_j+\lambda_k+\lambda_l\big) \\
&\quad + \cos\big((j-k)x+(k-l)y-\lambda_j+\lambda_k-\lambda_l\big) \\
&\quad - \cos\big((j+k)x+(l-k)y-\lambda_j-\lambda_k+\lambda_l\big) \\
&\quad - \cos\big((j+k)x-(k+l)y-\lambda_j-\lambda_k-\lambda_l\big)\Big]
\end{aligned} \tag{B.13}
$$

$$
\begin{aligned}
a_1b_2c_1 &= \sin(jx-\lambda_j)\cos(kx-ky-\lambda_k)\sin(ly-\lambda_l) \\
&= \frac{1}{4}\Big[\cos\big((j+k)x-(k+l)y-\lambda_j-\lambda_k-\lambda_l\big) \\
&\quad - \cos\big((j+k)x+(l-k)y-\lambda_j-\lambda_k+\lambda_l\big) \\
&\quad + \cos\big((j-k)x+(k-l)y-\lambda_j+\lambda_k-\lambda_l\big) \\
&\quad - \cos\big((j-k)x+(k+l)y-\lambda_j+\lambda_k+\lambda_l\big)\Big]
\end{aligned} \tag{B.14}
$$

$$
\begin{aligned}
a_2b_1c_1 &= \cos(jx-\lambda_j)\sin(kx-ky-\lambda_k)\sin(ly-\lambda_l) \\
&= \frac{1}{4}\Big[\cos\big((j+k)x-(k+l)y-\lambda_j-\lambda_k-\lambda_l\big) \\
&\quad - \cos\big((j+k)x+(l-k)y-\lambda_j-\lambda_k+\lambda_l\big) \\
&\quad + \cos\big((j-k)x+(k+l)y-\lambda_j+\lambda_k+\lambda_l\big) \\
&\quad - \cos\big((j-k)x+(k-l)y-\lambda_j+\lambda_k-\lambda_l\big)\Big]
\end{aligned} \tag{B.15}
$$

$$
\begin{aligned}
a_1b_2c_2 &= \sin(jx-\lambda_j)\cos(kx-ky-\lambda_k)\cos(ly-\lambda_l) \\
&= \frac{1}{4}\Big[\sin\big((j+k)x+(l-k)y-\lambda_j-\lambda_k+\lambda_l\big) \\
&\quad + \sin\big((j+k)x-(k+l)y-\lambda_j-\lambda_k-\lambda_l\big) \\
&\quad + \sin\big((j-k)x+(k+l)y-\lambda_j+\lambda_k+\lambda_l\big) \\
&\quad + \sin\big((j-k)x+(k-l)y-\lambda_j+\lambda_k-\lambda_l\big)\Big]
\end{aligned} \tag{B.16}
$$

$$
\begin{aligned}
a_2b_1c_2 &= \cos(jx-\lambda_j)\sin(kx-ky-\lambda_k)\cos(ly-\lambda_l) \\
&= \frac{1}{4}\Big[\sin\big((j+k)x+(l-k)y-\lambda_j-\lambda_k+\lambda_l\big) \\
&\quad + \sin\big((j+k)x-(k+l)y-\lambda_j-\lambda_k-\lambda_l\big) \\
&\quad - \sin\big((j-k)x+(k+l)y-\lambda_j+\lambda_k+\lambda_l\big) \\
&\quad - \sin\big((j-k)x+(k-l)y-\lambda_j+\lambda_k-\lambda_l\big)\Big]
\end{aligned} \tag{B.17}
$$

$$
\begin{aligned}
a_2b_2c_1 &= \cos(jx-\lambda_j)\cos(kx-ky-\lambda_k)\sin(ly-\lambda_l) \\
&= \frac{1}{4}\Big[\sin\big((j+k)x+(l-k)y-\lambda_j-\lambda_k+\lambda_l\big) \\
&\quad - \sin\big((j+k)x-(k+l)y-\lambda_j-\lambda_k-\lambda_l\big) \\
&\quad + \sin\big((j-k)x+(k+l)y-\lambda_j+\lambda_k+\lambda_l\big) \\
&\quad - \sin\big((j-k)x+(k-l)y-\lambda_j+\lambda_k-\lambda_l\big)\Big]
\end{aligned} \tag{B.18}
$$

$$
\begin{aligned}
a_1b_1c_1 &= \sin(jx-\lambda_j)\sin(kx-ky-\lambda_k)\sin(ly-\lambda_l) \\
&= \frac{1}{4}\Big[\sin\big((j-k)x+(k+l)y-\lambda_j+\lambda_k+\lambda_l\big) \\
&\quad - \sin\big((j-k)x+(k-l)y-\lambda_j+\lambda_k-\lambda_l\big) \\
&\quad - \sin\big((j+k)x+(l-k)y-\lambda_j-\lambda_k+\lambda_l\big) \\
&\quad + \sin\big((j+k)x-(k+l)y-\lambda_j-\lambda_k-\lambda_l\big)\Big]
\end{aligned} \tag{B.19}
$$

$$
\begin{aligned}
&\mathrm{T}\left(a_2b_2c_2 - a_1b_1c_2 + a_1b_2c_1 + a_2b_1c_1\right) \\
&\quad = \sum_{j,k,l=0}^{N-1} \cos\big((j+k)x-(k+l)y-\lambda_j-\lambda_k-\lambda_l\big)
\end{aligned} \tag{B.20}
$$

$$
\begin{aligned}
&a_1b_2c_2 + a_2b_1c_2 - a_2b_2c_1 + a_1b_1c_1 \\
&\quad = \sin\big((j+k)x-(k+l)y-\lambda_j-\lambda_k-\lambda_l\big)
\end{aligned} \tag{B.21}
$$

$$0 = \sum_{j,k,l,p=0}^{N-1} \sin\left((k-l)\frac{2\pi n}{N} + (j-k)\frac{2\pi m}{N} + \lambda_{jklp}\right) - \tan\left(\frac{2\pi nm}{N}\right)\cos\left((k-l)\frac{2\pi n}{N} + (j-k)\frac{2\pi m}{N} + \lambda_{jklp}\right) \tag{B.22}$$

Appendix C: Transformation matrices

$$U^{\#1}_{1,1} = \frac{1}{2} + \frac{e^{-i\beta/2}}{2\Theta}\left(\Theta\cos(\Theta/2) + \beta\sin(\Theta/2)\right) \tag{C.1a}$$

$$U^{\#1}_{1,2} = -\frac{2i\theta}{\Theta}e^{-i\beta/2}\sin(\Theta/2) \tag{C.1b}$$

$$U^{\#1}_{1,3} = -\frac{1}{2} + \frac{e^{-i\beta/2}}{2\Theta}\left(\Theta\cos(\Theta/2) + \beta\sin(\Theta/2)\right) \tag{C.1c}$$

$$U^{\#1}_{2,2} = e^{-i\beta/2}\left(\cos(\Theta/2) - i\frac{\beta}{\Theta}\sin(\Theta/2)\right), \tag{C.1d}$$

$$\Theta = \sqrt{\beta^2 + 8\theta^2} \tag{C.1e}$$

$$U^{\#2}_{11} = e^{-i(\theta+\beta)/2}\left(\cos(\Theta/2) + i\frac{\theta+\beta}{\Theta}\sin(\Theta/2)\right), \tag{C.2a}$$

$$U^{\#2}_{12} = -\frac{2\theta i}{\Theta}e^{-i(\theta+\beta)/2}\sin(\Theta/2) \tag{C.2b}$$

$$U^{\#2}_{22} = \frac{e^{-i(\theta+2\beta)/2}}{2}\left[e^{3i\theta/2} + e^{i\beta/2}\cos(\Theta/2) - i\frac{\theta+\beta}{\Theta}e^{i\beta/2}\sin(\Theta/2)\right] \tag{C.2c}$$

$$U^{\#2}_{23} = \frac{e^{-i(\theta+2\beta)/2}}{2}\left[e^{3i\theta/2} - e^{i\beta/2}\cos(\Theta/2) + ie^{i\beta/2}\frac{\theta+\beta}{\Theta}\sin(\Theta/2)\right] \tag{C.2d}$$

$$\Theta = \sqrt{8\theta^2 + (\theta+\beta)^2}$$

$$U^{\#3}_{11} = \frac{e^{-i(\Theta+\theta_2+\beta)/2}}{2\Theta}\left(\Theta - \theta_2 + \beta + e^{i\Theta}(\Theta + \theta_2 - \beta)\right), \tag{C.3a}$$

$$U^{\#3}_{12} = -\frac{2ie^{-i(\theta_2+\beta)/2}}{\Theta}\theta_1\sin(\Theta/2), \tag{C.3b}$$

$$U^{\#3}_{23} = \frac{e^{-i(\Theta+\theta_2+\beta)/2}}{4\Theta}\left(\Theta + \theta_2 - \beta + e^{i\Theta}(\Theta - \theta_2 + \beta) - 2\Theta e^{i(\Theta+3\theta_2+\beta)/2}\right), \tag{C.3c}$$

$$U^{\#3}_{33} = \frac{e^{-i(\Theta+\theta_2+\beta)/2}}{4\Theta}\left(\Theta + \theta_2 - \beta + e^{i\Theta}(\Theta - \theta_2 + \beta) + 2\Theta e^{i(\Theta+3\theta_2+\beta)/2}\right), \tag{C.3d}$$

$$\Theta = \sqrt{8\theta_1^2 + (\theta_2 - \beta)^2}.$$

[1] M.-A. Delsuc and P. O'Connor, Nature Reviews Methods Primers **4**, 49 (2024).
[2] J. W. Cooley and J. W. Tukey, Mathematics of Computation **19**, 297 (1965).
[3] I. J. Good, Journal of the Royal Statistical Society: Series B (Methodological) **20**, 361 (2018).
[4] V. Lyubashenko and S. Majid, Journal of Algebra **166**, 506 (1994).
[5] P. Shor, in *Proceedings 35th Annual Symposium on Foundations of Computer Science* (1994) pp. 124–134.
[6] P. Høyer, Phys. Rev. A **59**, 3280 (1999).
[7] A. Shakeel, Quantum Information Processing **19**, 10.1007/s11128-020-02834-y (2020).
[8] M. A. Nielsen and I. L. Chuang, *Quantum Computation and Quantum Information: 10th Anniversary Edition* (Cambridge University Press, 2010).
[9] P. Q. Le, F. Dong, and K. Hirota, Quantum Information Processing **10**, 63–84 (2010).
[10] N. Jain, J. Landman, N. Mathur, and I. Kerenidis, Quantum Science and Technology **9**, 035026 (2024).
[11] P. García-Molina, J. Rodríguez-Mediavilla, and J. J. García-Ripoll, Phys. Rev. A **105**, 012433 (2022).
[12] V. Dixit and S. Jian, Scientific Reports **12**, 10.1038/s41598-021-04639-0 (2022).
[13] C. Moore and M. Nilsson, SIAM Journal on Computing **31**, 799 (2001).
[14] R. Cleve and J. Watrous, in *Proceedings 41st Annual Symposium on Foundations of Computer Science* (2000)

pp. 526–536.
[15] D. R. Musk, Computing in Science & Engineering **22**, 103–110 (2020).
[16] F. Flamini, N. Viggianiello, T. Giordani, M. Bentivegna, N. Spagnolo, A. Crespi, G. Corrielli, R. Osellame, M. A. Martin-Delgado, and F. Sciarrino, Journal of Optics **20**, 074001 (2018).
[17] C. You, S. Adhikari, Y. Chi, M. L. LaBorde, C. T. Matyas, C. Zhang, Z. Su, T. Byrnes, C. Lu, J. P. Dowling, and J. P. Olson, Journal of Optics **19**, 124002 (2017).
[18] Z.-E. Su, Y. Li, P. P. Rohde, H.-L. Huang, X.-L. Wang, L. Li, N.-L. Liu, J. P. Dowling, C.-Y. Lu, and J.-W. Pan, Phys. Rev. Lett. **119**, 080502 (2017).
[19] F. Di Colandrea, N. Dehghan, A. D'Errico, and E. Karimi, npj Quantum Information **10**, 10.1038/s41534-024-00844-7 (2024).
[20] A. Mokeev, B. Saif, M. D. Lukin, and J. Borregaard, Enhancing optical imaging via quantum computation (2025).
[21] R. Ionicioiu, Scientific Reports **6**, 10.1038/srep25356 (2016).
[22] M. C. Tichy, K. Mayer, A. Buchleitner, and K. Mølmer, Phys. Rev. Lett. **113**, 020502 (2014).
[23] M. Reck, A. Zeilinger, H. J. Bernstein, and P. Bertani, Phys. Rev. Lett. **73**, 58 (1994).
[24] W. R. Clements, P. C. Humphreys, B. J. Metcalf, W. S. Kolthammer, and I. A. Walmsley, Optica **3**, 1460 (2016).
[25] R. Barak and Y. Ben-Aryeh, J. Opt. Soc. Am. B **24**, 231 (2007).
[26] Y. Li and F. Monticone, Nature Communications **16**, 10.1038/s41467-025-63453-8 (2025).
[27] A. Crespi, R. Osellame, R. Ramponi, M. Bentivegna, F. Flamini, N. Spagnolo, N. Viggianiello, L. Innocenti, P. Mataloni, and F. Sciarrino, Nature Communications **7**, 10.1038/ncomms10469 (2016).
[28] G. N. M. Tabia, Phys. Rev. A **93**, 012323 (2016).
[29] S. Rojas-Rojas, C. Muñoz, E. Barriga, P. Solano, A. Delgado, and C. Hermann-Avigliano, Phys. Rev. Res. **6**, 033224 (2024).
[30] M. Żukowski, A. Zeilinger, and M. A. Horne, Phys. Rev. A **55**, 2564 (1997).
[31] N. Spagnolo, C. Vitelli, L. Aparo, P. Mataloni, F. Sciarrino, A. Crespi, R. Ramponi, and R. Osellame, Nature Communications **4**, 10.1038/ncomms2616 (2013).
[32] A. Peruzzo, A. Laing, A. Politi, T. Rudolph, and J. L. O'Brien, Nature Communications **2**, 10.1038/ncomms1228 (2011).
[33] N. Spagnolo, L. Aparo, C. Vitelli, A. Crespi, R. Ramponi, R. Osellame, P. Mataloni, and F. Sciarrino, Scientific Reports **2**, 10.1038/srep00862 (2012).
[34] J. Cariñe, G. Cañas, P. Skrzypczyk, I. Šupić, N. Guerrero, T. Garcia, L. Pereira, M. A. S. Prosser, G. B. Xavier, A. Delgado, S. P. Walborn, D. Cavalcanti, and G. Lima, Optica **7**, 542 (2020).
[35] A. Ahmadi, R. Belk, C. Tamon, and C. Wendler, Quantum Information and Computation **3**, 611–618 (2003).
[36] A. Chan, Algebraic Combinatorics **3**, 757–774 (2020).
[37] P. Dita, Journal of Physics A: Mathematical and General **37**, 5355 (2004).
[38] S. Rojas-Rojas, E. Barriga, C. Muñoz, P. Solano, and C. Hermann-Avigliano, Phys. Rev. A **100**, 023841 (2019).
[39] W. Tadej and K. Życzkowski, Open Systems & amp; Information Dynamics **13**, 133–177 (2006).
[40] D. Cvetković and M. Petrić, Discrete Mathematics **50**, 37 (1984).
[41] A. Alberucci, N. Alasgarzade, M. Chambonneau, M. Blothe, H. Kämmer, G. Matthäus, C. P. Jisha, and S. Nolte, Phys. Rev. Appl. **14**, 024078 (2020).
[42] F. L. Kien, L. Ruks, S. N. Chormaic, and T. Busch, New J. Phys. **22**, 10.1088/1367-2630/abc8af (2020).